Volume 13
Number 1
7 January 2025
Pages 1-334

Biomaterials Science

rsc.li/biomaterials-science

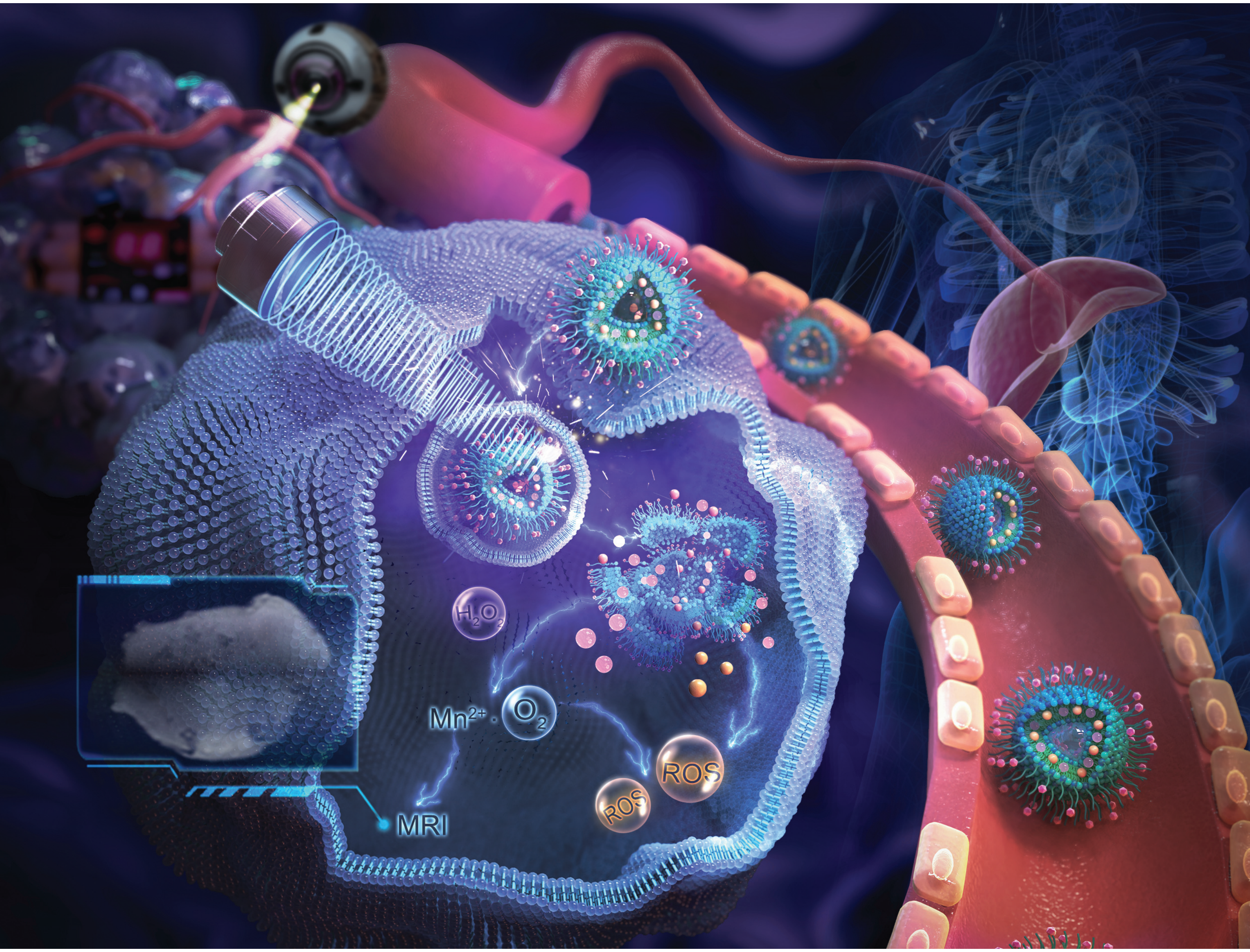

ISSN 2047-4849

PAPER
Yun Chen, Xintao Shuai, Guanxun Cheng, Li Liu, Tingting Zheng *et al.*
Use of UMFNPs/Ce6@MBs in multimodal imaging-guided sono-photodynamic combination therapy for hepatocellular carcinoma

ROYAL SOCIETY
OF **CHEMISTRY**

European
Society for
Biomaterials

Biomaterials Science

ROYAL SOCIETY OF CHEMISTRY

PAPER

View Article Online
View Journal | View Issue

Check for updates

Cite this: *Biomater. Sci.*, 2025, **13**, 179

Received 3rd May 2024,
Accepted 17th October 2024

DOI: 10.1039/d4bm00613e

rsc.li/biomaterials-science

Use of UMFNPs/Ce6@MBs in multimodal imaging-guided sono-photodynamic combination therapy for hepatocellular carcinoma†

Lijun Xing,‡[a,b] Xiaoting Yang,‡[a] Jianhua Bai,‡[a] Chunting Zhong, ‡[a] Jing Cai,‡[c] Qing Dan,[a] Yiran Ji,[a] Bingxuan Xu,[a] Keyan Yu,[d] Xiaoyu Chen,[a] Yulong Qi,[d] Li Li,[e] Yun Chen,*[a] Xintao Shuai, *[f] Guanxun Cheng,*[d] Li Liu*[a] and Tingting Zheng *[a]

Early diagnosis of liver cancer and appropriate treatment options are critical for obtaining a good prognosis. However, due to technical limitations, it is difficult to make an early and accurate diagnosis of liver cancer, and the traditional imaging model is relatively simple. Therefore, we synthesized multifunctional diagnostic/therapeutic nanoparticles, UMFNPs/Ce6@MBs, loaded with ultra-small manganese ferrite nanoparticles (UMFNPs) and chlorin e6 (Ce6). This nanoplatform can take full advantage of hypoxia, acidic pH (acidosis) and increased levels of reactive oxygen species (*e.g.* H_2O_2) in the tumor microenvironment (TME). Specific imaging and drug release can also enhance tumor therapy by modulating the hypoxic state of the TME to achieve the combined effect of sonodynamic therapy and photodynamic therapy (SPDT). In addition, the prepared UMFNPs/Ce6@MBs have H_2O_2 and pH-sensitive biodegradability and can release UMFNPs and photosensitizer Ce6 in the TME while producing O_2 and Mn^{2+}. The obtained Mn^{2+} ion nanoparticles can be used for T_1 magnetic resonance imaging of tumor-bearing mice, and the released Ce6 can provide fluorescence imaging function at the same time. Because UMFNPs/Ce6@MB ultrasonic microbubbles show good ultrasonic imaging results, UMFNPs/Ce6@MBs can simultaneously provide multi-modal imaging functions for magnetic resonance imaging (MRI), ultrasound and fluorescence imaging. In conclusion, UMFNPs/Ce6@MBs realize the synergistic treatment of SDT and PDT under multi-mode near-infrared fluorescence imaging and CEUS monitoring, demonstrating its great potential in tumor precision medicine.

1. Introduction

Liver cancer is one of the most common malignancies worldwide. According to the Global Cancer Statistics 2020, the global increase in new liver cancer cases now exceeds 0.9 million cases annually.[1] Currently, the main treatment modalities for liver cancer include radical surgery, local ablation, arterial embolization, radiotherapy, and systemic chemotherapy. Because hepatocellular carcinoma (HCC) is usually diagnosed at an advanced stage, its prognosis is poor and its mortality rate is high. Early HCC tends to lack clinical signs; therefore, only 25%–30% of patients with HCC are diagnosed at the early stage of the disease and only 5%–15% of patients are suitable for surgical resection.[2,3] Advanced HCC is mainly treated using targeted therapy and immunotherapy but the treatment outcomes are still poor and there are many side effects.[4] Therefore, there is an urgent need to identify new and effective methods for diagnosing and treating liver cancer.

---

[a] *Shenzhen Key Laboratory for Drug Addiction and Medication Safety, Department of Ultrasound, Institute of Ultrasonic Medicine, Peking University Shenzhen Hospital, Shenzhen Peking University-The Hong Kong University of Science and Technology Medical Center, Shenzhen 518036, Guangdong, P. R. China. E-mail: yunchen@sphmc.org, liuli@pkuszh.com, kyzs_018@126.com*

[b] *Department of Hubei University of Medicine, Wuhan 430000, Hubei, P. R. China*

[c] *Guangdong Provincial Key Laboratory of Malignant Tumor Epigenetics and Gene Regulation, Guangdong-Hong Kong Joint Laboratory for RNA Medicine, Medical Research Center, Sun Yat-sen Memorial Hospital, Sun Yat-sen University, Guangzhou, 510000 Guangdong, P.R. China*

[d] *Department of Medical Imaging, Peking University Shenzhen Hospital, Shenzhen 518036, Guangdong, P. R. China. E-mail: chengguanxun@hotmail.com*

[e] *Department of Medical Imaging, State Key Laboratory of Oncology in South China, Collaborative Innovation Center for Cancer Medicine, Sun Yat-sen University Cancer Center, Sun Yat-sen University, Guangzhou 510000, China*

[f] *PCFM Lab of Ministry of Education, School of Materials Science and Engineering, Sun Yat-Sen University, Guangzhou 510275, Guangdong, P. R. China. E-mail: shuaixt@ mail.sysu.edu.cn*

† Electronic supplementary information (ESI) available. See DOI: **https://doi.org/10.1039/d4bm00613e**

‡ These authors contributed equally.

Traditional imaging modes alone cannot completely detect liver cancer early and improve its prognosis. However, the diagnostic methods for liver cancer are continuously improving and developing, and good results have been achieved. Among the many medical imaging methods, magnetic resonance imaging (MRI) and ultrasonography are the most valuable early diagnostic tools currently used in medicine. In recent years, in-depth studies on molecular MRI (mMRI) in gene imaging, cell tracking, and drug screening have been conducted and have exceeded traditional MRI techniques in terms of improving the rate of early diagnosis and the therapeutic effect.[5] Recent studies have demonstrated that ultrasmall magnetic ferrite nanoparticles (UMFNPs), which are <5 nm, have strong MRI-T_1 imaging effects and can be encapsulated with other targeted therapy drugs to achieve precise treatment during diagnosis.[6] This demonstrates the strengths of ultrasound microbubbles. Microbubbles can encapsulate nanoparticles for precise delivery to the lesion site. Upon arrival at the target site, these microbubbles burst and release drugs through sonoporation, and the CEUS effect of the lesion site can be dynamically observed in the whole process under the condition of visualization. Routine ultrasound has a diagnostic accuracy of 53%–77% for larger space-occupying lesions in the liver. The use of contrast agent microbubbles during contrast-enhanced ultrasound (CEUS) can reveal smaller liver lesions (≤1 cm) and has higher diagnostic accuracy.[7,8]

Photodynamic therapy (PDT) is a non-invasive and relatively safe local treatment for tumors that has attracted widespread attention in recent years. PDT mainly generates reactive oxygen species (ROS), which mediate their killing effects through laser excitation of the photosensitizer.[9] Certain levels of ROS can promote tumorigenesis, but excessive accumulation of singlet oxygen and oxygen free radicals has significant cytotoxic effects on cancer cells, preventing their growth and inducing death.[10,11] Despite the fact that PDT is extensively used in treating cancers such as breast, oropharyngeal, esophageal, and skin cancers, the weak penetration of PDT has limited its value in the clinical treatment of deep tumors. To improve the efficacy of PDT, it has been increasingly combined with other treatments, such as sonodynamic treatment (SDT), to treat deep tumors, liver cancer,[9,12] and bone tumors.[13] SDT has stronger penetration, can activate sonosensitizers in deep tumors, and can similarly generate free radicals that cause cell death and compensate for the shortcomings of PDT to some extent. Chlorin e6 (Ce6) is a second-generation sensitizer with both sonosensitizer and photosensitizer characteristics. Because of its high singlet oxygen generation rate, low toxicity, and near-infrared emission characteristics, it is widely studied in sono-photodynamics and fluorescence (FL) imaging. However, the water solubility, poor stability, poor tumor targeting, and synthesis difficulty of Ce6 severely limit its further application in clinical practice.[14] In an attempt to solve this problem, we developed a multi-functional nanoplatform (UMFNPs/Ce6@MBs) combined with the SPDT therapy strategy for HCC, as shown in Scheme 1. Ce6 and UMFNPs were encapsulated in phospholipid microvesicles, and the targeted cyclic

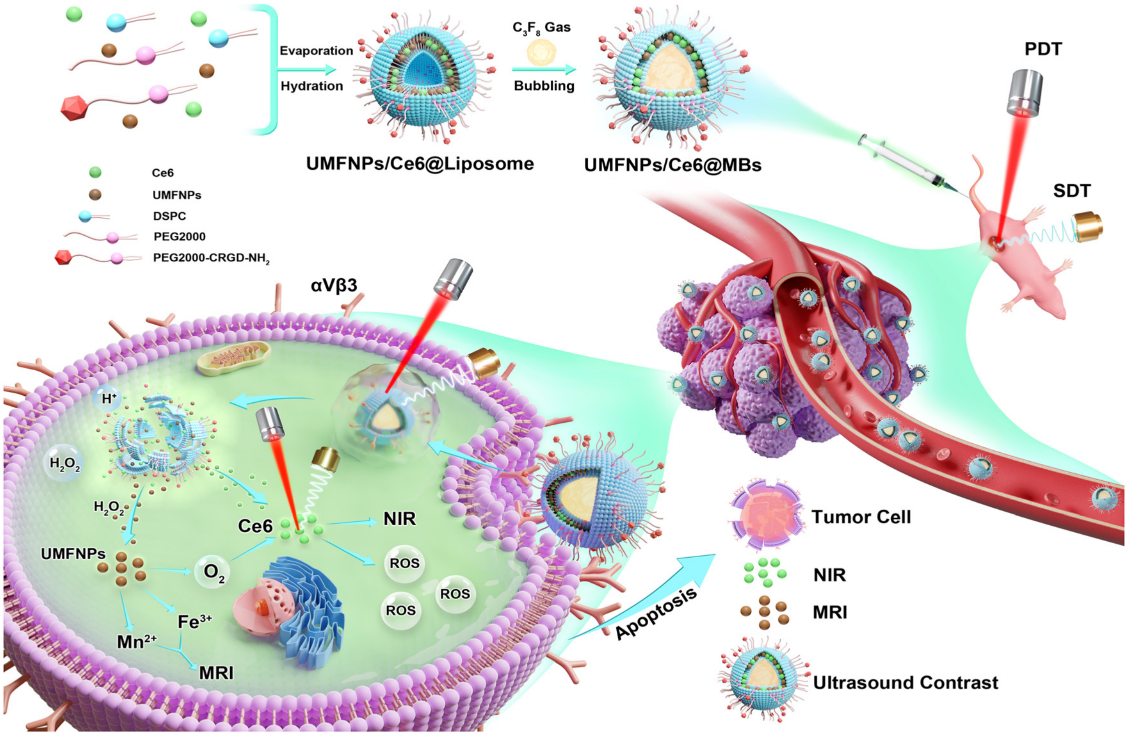

Scheme 1 Schematic diagram of the synthesis process of UMFNPs/Ce6@MBs and the mechanism of triggering MRI/FL imaging/enhanced ultrasound guided SDT/PDT combination therapy for HCC.

peptide C-RGD was modified on the surface of the microvesicles, which can improve the bioavailability of drugs at the tumor site. The therapeutic effect of SPDT on HCC was further enhanced by O_2 generated in response to the weak acidic microenvironment of tumor. In addition, UMFNPs/Ce6@MBs can realize multi-modal imaging integrating CEUS, FLI and T_1-MRI for accurate diagnosis and treatment guidance of liver cancer. As our research group's previous preparation technology of microvesicles was mature enough and the prepared microvesicles achieved good effects in precision drug delivery and tumor treatment, UMFNPs/Ce6@MBs prepared on the basis of previous studies were relatively reliable and had great potential in realizing accurate and efficient treatment of HCC.[15–19]

2. Materials and methods

2.1. Materials

Poly(ethylene glycol)-distearoylphosphatidylethanolamine (PEG-2000) and distearoylphosphatidylcholine (DSPC) were purchased from Avanti Inc. (USA); PEG2000-CRGD-NH2 was purchased from Xi'an Ruixi Biological Technology Co., Ltd; Ce6, DMEM, 0.25% trypsin (TE), fetal bovine serum (FBS), and 1% penicillin/streptomycin (1% penicillin and 1% streptomycin) were purchased from Gibco Inc. (USA); Huh-7 cells (FH0075 FuHeng Cell Center, Shanghai, China). The ROS fluorescent probe was purchased from Invitrogen Inc. (USA); phosphate-buffered saline (PBS) was purchased from Sigma-Aldrich Inc. (USA); carbon tetrachloride (CCl^4) was purchased from Guangdong Huada Chemical Factory; 4% paraformaldehyde was purchased from Biosharp (China); ready-to-use DAPI staining solution was purchased from Solarbio (China); and the cytotoxicity assay kit (CCK-8) was purchased from Beijing Labgic Technology (China).

2.2. UMFNPs preparation and characterization

Iron-eruciate and manganese oleate precursors were prepared according to the methods of Fan *et al.* and Miao *et al.*[6,20] They were provided by the Affiliated Cancer Hospital of Sun Yat-sen University. Dynamic simultaneous thermal decomposition was used to prepare ultra-small manganese ferrite nanoparticles. It was prepared by the following preparation method: 2.7 g iron oleate, 8.1 g erucic acid and 1.08 g sodium hydroxide were dissolved in 150 mL of methanol, and the reaction was carried out by magnetic stirring at 40 °C. After the reaction was completed, the products were washed with deionized water and methanol, and the obtained products were dried under vacuum at 45 °C for 12 hours to obtain the iron erucic acid complex; 2.14 g of the ferric erulic acid complex, 0.62 g of the manganoleic acid complex, 0.57 g oleic acid, and 1.61 g oleyl alcohol were dissolved in 10 g of the benzyl ether solvent, and then the reaction mixture was heated to 265 °C and kept at this temperature for 35 min. After the reaction, the reaction mixture was cooled, washed with ethanol, and centrifuged to obtain UMFNPs.

2.3. Preparation and characterization of UMFNPs/Ce6@MBs

DSPC, PEG 2000, and C-RGD were dissolved in chloroform at a molar ratio of 18 : 2 : 2. UMFNPs (1 mg mL^{-1}) : Ce6 (2 mg mL^{-1}) was dissolved in a 1 : 1 ratio in the aforementioned chloroform to form a lipid phase. To prepare UMFNPs/Ce6@MBs, 150 μL of DSPC, 150 μL of PEG-2000, 150 μL of C-RGD, 125 μL of Ce6, and 125 μL of UMFNPs were mixed in a thumb bottle and placed on a rotary evaporator in a fume hood for 30 min of rotary evaporation to form a lipid membrane. Then, 500 μL of PBS was added for hydration, and sonication was performed in a 60 °C water bath for 3–5 min. The hydrated liposome was transferred to a vial and sealed before inserting a syringe through the rubber stopper and connecting to a small vial for gaseous exchange.

First, the air inside the vial was removed for 5 min under vacuum. Then, octafluoropropane (C_3F_8) gas was added, the vial was tapped for 1 min to mix the gas, and air suction was performed for 5 s. To ensure complete gaseous exchange, this process was repeated 3–5 times. Subsequently, C_3F_8 was added and a shaker was used for 45 s to form UMFNPs/Ce6@MBs. A dynamic light scattering measurement system (DLS) was used to measure the fluid dynamics diameter and charge of UMFNPs/Ce6@MBs. A particle analyzer (AccuSizer 780AD) was used to measure the size, particle size distribution, and concentration before observing the structure under an optical microscope. An ultraviolet spectrophotometer was used to measure the ultraviolet absorption spectra of MBs, Ce6, and UMFNPs.

2.4. *In vitro* anti-tumor effect

2.4.1. Evaluation of cell viability. Huh-7 cells (derived from human hepatocytes) were purchased from Procell Life Science & Technology. The cells were cultured in DMEM containing 10% FBS and 1% penicillin/streptomycin. The cells were seeded in 96-well plates at a density of 2 × 10^4 and cultured in an incubator at 37 °C under 5% CO_2. When the cells reached a confluency of 70%–80%, DMEM culture medium was used to dilute the UMFNPs/Ce6@MBs to a gradient concentration of 0, 5, 10, 15, and 20 μg mL^{-1}. Next, 100 μL of the replacement culture medium was aspirated and each concentration was plated in triplicate, and corresponding ultrasonic and laser treatments were conducted; the ultrasound (LIPUSTIM Sonodynamic Therapy System, LIPU.STIM330) conditions were as follows: frequency, 1.0 MHz; duty ratio, 20%; pulse frequency, 1000 Hz; magnetic reluctance intensity, 500 mW cm^{-2}. The laser (LASER POWER SUPPLYMODEL NO.: LSR-PS-II) conditions were as follows: 660 nm, 150 mW cm^{-2}, 1 min. After 24 h, the cell viability was measured using a CCK-8 assay kit (Biosharp, Anhui) according to the manufacturer's instructions. The optimal concentration was selected and the cells were divided into five groups, namely control, UMFNPs/Ce6@MBs, UMFNPs/Ce6@MBs + SDT, UMFNPs/Ce6@MBs + PDT, and UMFNPs/Ce6@MBs + SPDT, and the corresponding measurements were performed before measuring the cell viability.

2.4.2. Anti-tumor effect of UMFNPs/Ce6@MBs + SPDT. The apoptosis of MnO_2 /Ce6@MBs + SPDT cells was detected by flow cytometry. Huh-7 cells were inoculated into 6-well plates at a density of 2×10^5 per well and incubated overnight. After administration, ultrasound and laser treatment were performed, and the Annexin V-FITC/PI reagent was added for further incubation for 30 min. After PBS washing, trypsin digestion, and centrifugation (3000 rpm, 10 min), the cells were collected for flow cytometry. The data were analyzed using the Flowjo program.

2.5. Measurement of ROS generation at the cellular level

Huh-7 cells were seeded in a 6-well plate and confocal dish at a density of 1×10^5. After 24 h of incubation, the culture medium was discarded and 1.5 mL of UMFNPs/Ce6@MBs (15 μg mL^{-1}) was added. The corresponding ultrasound and laser treatments were performed, and incubation was continued for 4 h. The culture medium was discarded and a DCFH-DA ROS probe with a diluted concentration of 20 μmol L^{-1} (2 μL ROS + 1 mL PBS) was added. Next, 1 mL of the ROS probe was added to every example and cultured at 37 °C for 30 min. The tubes were centrifuged, the supernatant was discarded, and 500 μL of PBS was added. Tubes with untreated cells were used as controls. A laser confocal microscope and a flow cytometer were used to measure the generation of ROS at the cellular level.

2.6. Cell uptake of UMFNPs/Ce6@MBs

2.7. Animal rearing

We used the fluorescence properties of Ce6 in UMFNPs/Ce6@MBs to test the uptake of microvesicles by Huh-7 cells. Huh-7 cells were seeded in a confocal dish at a density of 1×10^5. After 24 h of incubation, when the cell density was 60%–80%, the culture medium was discarded and 1 mL of UMFNPs/Ce6@MBs (Ce6 15 μg mL^{-1}, UMFNPs 7.5 μg mL^{-1}) was added. The corresponding ultrasound and laser treatments were performed, and the incubation was continued for 4 h. The cells were washed twice with PBS before adding the ROS solution (2 μL ROS probe + 1 mL PBS) and incubating for 30 min. The ROS probe was discarded, and PBS was used to wash the cells 1–2 times. Finally, 400 μL of DAPI was used for fixation, and confocal microscopy was performed at 4 h.

All animal experiments were conducted according to the “Laboratory Animal Welfare Act” and were approved by the Laboratory Animal Welfare Ethics Committee of Shenzhen-Peking University – The Hong Kong University of Science and Technology Medical Center. BALB/c mice (4–6 weeks old, males) were purchased from Charles River and housed at 25 °C, 40%–60% humidity, and a 12 h light/dark cycle.

2.8. *In vivo* anti-cancer treatment effects

Six experimental groups were set up: the control group, the model group, the UMFNP/Ce6@MB group, the UMFNP/Ce6@MB + SDT group, the UMFNP/Ce6@MB + PDT group, and the UMFNP/Ce6@MB + SPDT group. With the exception of the control group, in which normal nude mice were used, the remaining groups were all tumor-bearing mice. The control, model, and UMFNP/Ce6@MB groups each contained six nude mice, whereas the other three groups each contained eight mice. All mice were subcutaneously injected with 5×10^6 Huh-7 cells in the posterior thigh region. Treatment was started when the tumor size was 5 mm, and 0.2 mL of UMFNPs/Ce6@MBs (Ce6 15 μg mL^{-1} and UMFNPs 7.5 μg mL^{-1}) was injected into the tail vein of nude mice. Then, focused ultrasound (power amplifier model: 150A100B, probe model: 122121001) was performed for the SDT and SPDT groups (parameters: 0.8 MHz, 900 mVpp, 10 000 cycles, 10 min), and laser treatment was performed for the PDT and SPDT groups (parameters: 660 nm, 800 mW cm^{-2}, 10 min). The treatment cycle lasted 2 weeks, with dosing being performed every other day. The body weight was also measured every other day while simultaneously measuring the tumor size with an ultrasound device. The following formula was used to calculate the tumor volume: $V = (a \times b^2)/2$ (where a = maximum tumor diameter and b = minimum tumor diameter).

After treatment, the mice were sacrificed to harvest tumor tissues, which were then fixed with 10% formalin for 24 h. The samples then underwent paraffin embedding, sectioning, clearing, rehydration, and staining before observing Ki-67 expression under an optical microscope.

2.9. *In vivo* imaging

2.9.1. FL imaging and C-RGD tumor-targeting capacity measurement. After the intravenous injection of 0.2 mL of UMFNPs/Ce6@MBs (with C-RGD), the mice were imaged using the IVIS spectrum imaging system (Caliper IVIS Spectrum, IVIS) before injection and 5 min, 30 min, 1 h, 4 h, 12 h, and 24 h after injection of microbubbles (the fluorescence excitation wavelength for Cy5.5 is 640 nm). The average FL intensity at the corresponding time point was obtained at the excitation wavelength of 640 nm. The fluorescence signal of the region of interest (ROI) was analyzed qualitatively and quantitatively using Living Image 4.2 software.

In addition, the targeting effects of C-RGD were measured using fluorescence imaging. Two groups were set up for the experiment, including the UMFNP/Ce6@MB (with C-RGD) and UMFNP/Ce6@MB-(non C-RGD) groups, with three subcutaneous tumor-bearing nude mice per group. In the same time period (pre, 5 min, 30 min, 1 h, 4 h, 8 h, 12 h, and 24 h), by comparing the fluorescence intensity of the two groups, the targeting effect of the modified C-RGD microvesicle on the tumor was analyzed.

2.9.2. US imaging. After the intravenous injection of UMFNPs/Ce6@MBs (200 μL), grayscale ultrasound and CEUS were performed on a US imaging system (Mindray Resona 7, China) at periods of 0, 0.5, 1, 3, 6, and 8 min, respectively.

2.9.3. MRI imaging. Briefly, 0.2 mL of UMFNPs/Ce6@MBs was administered to tumor-bearing mice (n = 3). MRI was performed before dosing and 1 min, 1 h, 2 h, and 3 h after dosing to obtain T_1-weighted MRI images of the tumor site. The MRI intensity of the tumor site was analyzed. The experimental parameters or the T_1 fast recovery spin-echo sequence were set as follows: repetition time = 279.2 ms, echo time = 2.3 ms, slice thickness = 2 mm.

2.10. *In vivo* safety assessment

Two weeks after treatment, inferior vena cava blood was collected and centrifuged to obtain serum. Different organs and tumor tissues were dissected and fixed with 10% formalin for 24 h, with untreated healthy mice used as controls. The collected serum, organs, and tumors were used for analysis. The serum obtained after centrifugation was used to measure liver function including aspartate aminotransferase (AST) and alanine aminotransferase (ALT) and renal function including creatinine (CREA) and blood urea nitrogen (BUN). Pathological changes in different organs and tumors were observed under an optical microscope.

2.11. Statistical analysis

All data are expressed as the mean ± standard deviation (SD). The *t*-test or analysis of variance was used to analyze statistical significance. *P*-Values <0.05 were considered to indicate significant differences: $*P < 0.05$, $**P < 0.01$, $***P < 0.001$, $****P < 0.0001$.

3. Results

3.1. UMFNP preparation and characterization

In this study, the main role of UMFNPs (containing 0.12 mg of Fe and 0.087 mg of Mn in each mg sample) was as a nanomaterial for providing Mn^{2+} and Fe^{3+} for MRI imaging. Under transmission electron microscopy (TEM), UMFNPs showed a narrow distribution and good uniformity (Fig. 1D), with a particle size of 3–5 nm (Fig. 1E). TEM images (Fig. 1D white dotted box) showed that the lattice had high crystallinity, proving that the structure of this nanomaterial is relatively stable. A 3.0-T clinical MRI scanner was used to evaluate T_1-enhanced imaging, and the FSE T1WI sequence was used to image the UMFNP solution. The T_1 imaging signal increased with the UMFNP concentration (Fig. 1G). To restore the slightly acidic environment of the tumor microenvironment, we prepared UMFNPs into liposomes at a concentration of 0.125 μg mL^{-1}, and added H_2O_2 at a concentration of 100 μmol mL^{-1} for MRI imaging, and the following results were obtained: (1) UMFNPs encapsulated in liposomes had stronger T_1 signals than UMFNPs alone, and (2) UMFNPs encapsulated in liposomes and imaged after H_2O_2 was added for 1 h had higher T_1 signals (Fig. 1H). Furthermore, a Malvern dynamic light scattering measurement system was used to measure the potential of UMFNPs, which was determined to be −48.18 mV, indicating that the charged Ce6 in microbubbles was stably bound to UMFNPs (Fig. 1C).

3.2. Preparation and characterization of UMFNPs/Ce6@MBs

First, the microbubbles were characterized by DLS. DLS showed that the particle size of the microbubbles was 1 μm (Fig. 1C), which was in the range of a typical microbubble size, allowing further biomedical applications. The particle size was consistent with the optical microscopy (Fig. 1A) and particle counter (Fig. 1B) results. Optical microscopy revealed that the microbubbles had a spherical structure and uniform dispersion, which could prevent *in vivo* clumping and allow better adaptation to the external environment. The particle count result also showed that the microbubble concentration was 4×10^{10} mL^{-1} (Fig. 1B). The ultraviolet absorption spectrum showed that the absorbance increased with increasing microbubble concentration and that UMFNPs almost did not absorb light (Fig. S1†). The main substance that absorbs light in UMFNPs/Ce6@MBs was Ce6. The characteristic peak of Ce6 shifted from 640 nm to 665 nm, indicating that Ce6 was stably encapsulated in the microbubbles (Fig. 1F).

3.3. Huh-7 cell culture and cytotoxicity evaluation of UMFNPs/Ce6@MBs

Huh-7 cells were seeded in 96-well plates in DMEM at a density of 2×10^4 and incubated in a 37 °C, 5% CO_2 humidified incubator for 24 h. The cells showed stable adherent growth, with a density of 70%–80%. DMEM culture medium was used to dilute UMFNPs/Ce6@MBs to a concentration gradient of 0, 5, 10, 15, and 20 μg mL^{-1}. A CCK-8 assay was used to measure the effects of different concentrations of UMFNPs/Ce6@MBs on cell viability. When the concentration was 15 μg mL^{-1}, the cell viability was ≥90%, while a concentration of 20 μg mL^{-1} resulted in cytotoxicity. Therefore, 15 μg mL^{-1} is the optimal concentration to ensure that the dosing concentration is within the absolute safe range (Fig. 2A).

3.4. *In vitro* anti-tumor effect

To examine the killing effects of UMFNPs/Ce6@MBs combined with sono-photodynamics on cells while avoiding significant effects on cell viability and morphology. The parameters of the ultrasound and laser irradiation were first determined. A dosing concentration of 15 μg mL^{-1} was used. The results showed that the cell survival rates in the UMFNPs/Ce6@MBs + SDT, UMFNPs/Ce6@MBs + PDT, and UMFNPs/Ce6@MBs + SPDT groups were 84%, 72%, and 64%, respectively (Fig. 2B), which were different from those in the control group. However, there was no significant difference between the UMFNP/Ce6@MB and control groups, indicating that ultrasound, laser, and their combination can kill Huh-7 liver cancer cells.

We also detected the effect of UMFNPs/Ce6@MBs combined with SPDT on the apoptosis of Huh-7 cells by flow cytometry. Total apoptosis, including early and late apoptosis, was analyzed after incubation with UMFNPs/Ce6@MBs (15 μg mL^{-1}) and then treated with SDT, PDT, or SPDT. In Fig. 3C and D, the apoptosis rate of UMFNPs/Ce6@MBs + SPDT reached 26%. As more Ce6 is taken up by Huh-7 cells and accumulates within tumor tissues, the anti-tumor ability will improve. The ability to kill cancer cells was significantly enhanced by improving targeted drug release, cell membrane penetration and cell uptake.

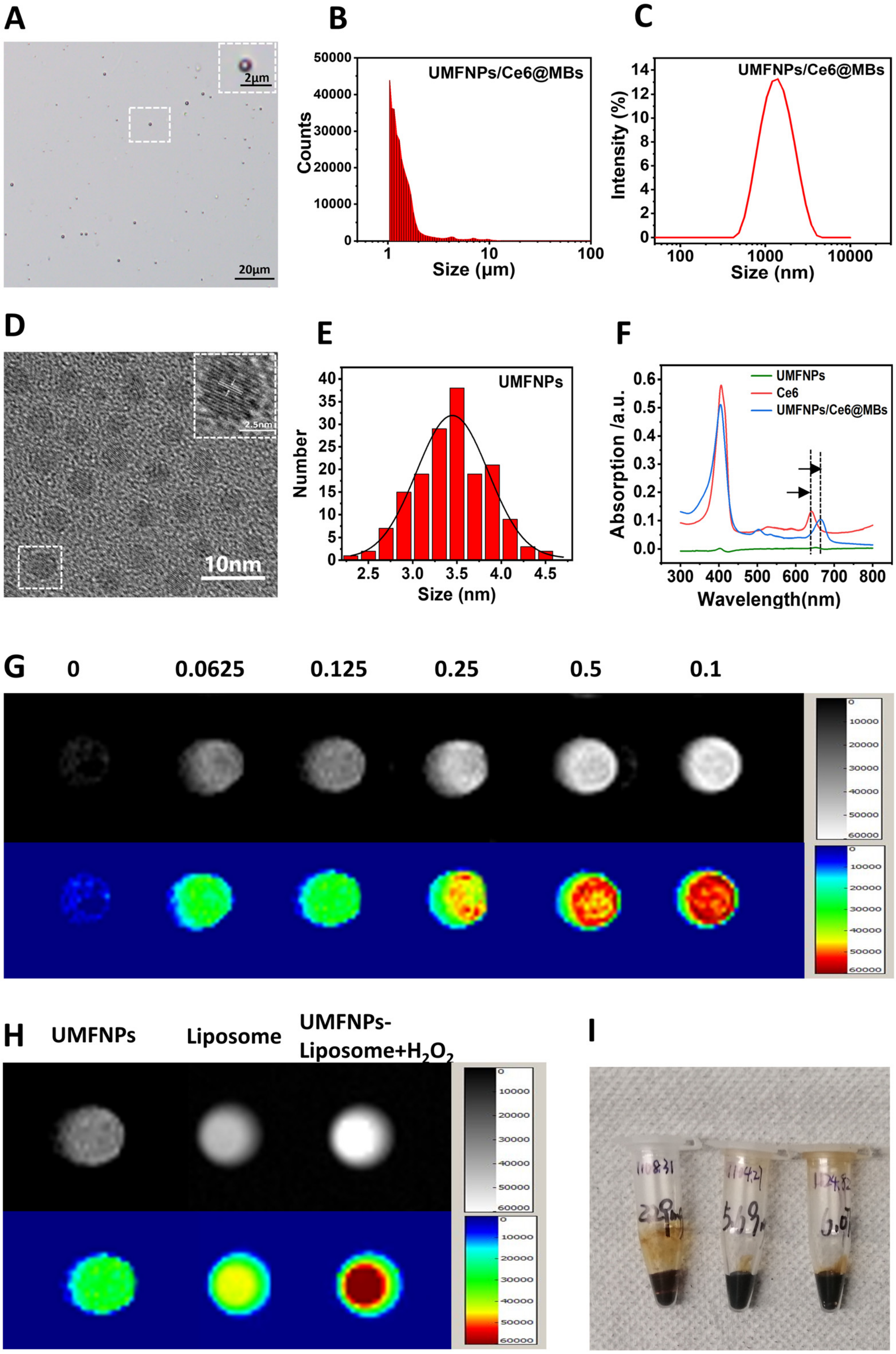

Fig. 1 Preparation and characterization of UMFNPs and UMFNPs/Ce6@MB. (A) The structures of UMFNPs/Ce6@MBs were observed using an optical microscope; an amplified view of typical UMFNPs/Ce6@MBs shown in the inset image (white rectangular with a dashed line). (B) The sizes of UMFNPs/Ce6@MBs were measured by PSS. (C) The sizes of UMFNPs/Ce6@MBs were measured by DLS. (D) The structure and distribution of UMFNPs were observed under a TEM, and the crystal structure of UMFNPs/Ce6@MBs is shown in the illustration (white rectangular with a dashed line). (E) UMFNPs' particle sizes. (F) Ultraviolet absorption spectrum of UMFNPs, Ce6, and UMFNPs/Ce6@MBs. (G) MRI-T_1 imaging results of the UMFNP solution at different concentrations (0, 0.0625, 0.125, 0.5, and 1 mg mL^{-1}). (H) MRI-T_1 imaging results after the reaction of UMFNPs and liposomes for 1 h. (I) Gross appearance of UMFNPs (imaging parameters: SF = 21 MHz, O1 = 232 246 Hz, RFA90° = 2.6, RFA180° = 3.9, TR = 200 ms, TE = 20 ms, slice width = 8 mm, slices = 1, average = 8, read size = 256, phase size = 192).

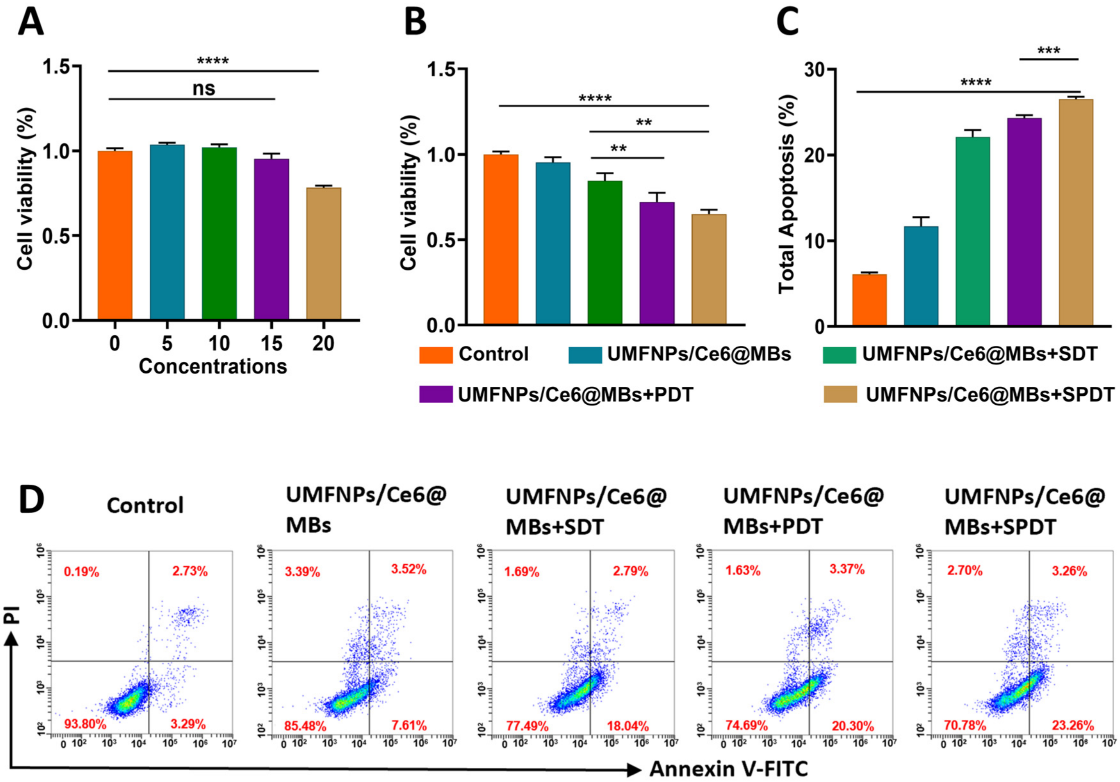

Fig. 2 Cytotoxicity and *in vitro* treatment evaluation of UMFNPs/Ce6@MBs. (A) Cytotoxicity of UMFNPs/Ce6@MB particles measured using the CCK-8 assay. (B) *In vitro* therapeutic effects of UMFNPs/Ce6@MBs measured using the CCK-8 assay. (C) Quantification of (D). (D) Huh-7 cell apoptosis assay by flow cytometry after the different treatments. $**p < 0.01$, $****p < 0.0001$.

3.5. Uptake and distribution of UMFNPs/Ce6@MBs in Huh-7 cells

To test whether microvacuoles are effectively absorbed by Huh-7 cells, we observed the absorption and distribution of UMFNPs/Ce6@MBs (equivalent to 15 μg mL^{-1} Ce6) in Huh-7 cells by confocal scanning imaging using multiplex staining, including nuclear and cytoskeleton imaging, based on the NIR properties of Ce6. We found that the cell nuclei were stained blue by DAPI, while clear Ce6 red fluorescence signals could be seen in the cytoplasm (Fig. 3C). No fluorescence signal of Ce6 was detected in the control group; however, compared to the control group, the UMFNP/Ce6@MB group showed significantly increased fluorescence intensity, which was evenly distributed in the cytoplasm. This result shows that Huh-7 cells effectively took up UMFNPs/Ce6@MBs and that UMFNPs/Ce6@MBs entered the cytoplasm of Huh-7 cells *via* endocytosis or macropinocytosis.

3.6. *In vitro* ROS generation capacity of UMFNPs/Ce6@MBs

ROS were quantitatively and qualitatively analyzed by cytometry and confocal microscopy, respectively, and ROS production was visualized in Huh-7 cells and Huh-7-tumor tissues by FL imaging. The results showed that the fluorescence intensity of ROS in the control group was very weak, and ROS could be produced in the experimental group UMFNPs/Ce6@MBs + SDT, UMFNPs/Ce6@MBs + PDT and UMFNPs/Ce6@MBs + SPDT after acoustic/photodynamic treatment (Fig. 3A, B, and D). The ROS produced by the UMFNP/Ce6@MB + SPDT group was significantly higher than those by UMFNPs/Ce6@MBs + SDT and UMFNPs/Ce6@MBs + PDT treated by ultrasound or laser alone, indicating that the combined action of SDT and PDT further enhanced the killing effect of ROS on tumor cells. In UMFNPs/Ce6@MBs + PDT, the Ce6 FL signal is enhanced, which may be due to the mild thermal effect of laser irradiation. UMFNPs/Ce6@MBs + SDT significantly enhanced the Huh-7 cell uptake of microvesicles due to the UTMD effect promoting UMFNPs/Ce6@MBs release and Huh-7 cell membrane penetration. UMFNPs/Ce6@MBs + SDT significantly enhanced the Huh-7 cell uptake of microvesicles due to the UTMD effect promoting the release of UMFNPs/Ce6@MBs and Huh-7 cell membrane penetration. Finally, combined with US and laser irradiation, Huh-7 cells exhibited the strongest Ce6 FL signal.

3.7. *In vivo* safety assessment

After 2 weeks of treatment, the mouse heart, liver, spleen, lungs, kidneys, and tumor-bearing tissues were harvested for HE staining. The sections were observed under an optical microscope, and the results are shown in Fig. 4A. Compared to the control group, the cells and tissues in organs from the experimental groups had an intact structure, without signifi-

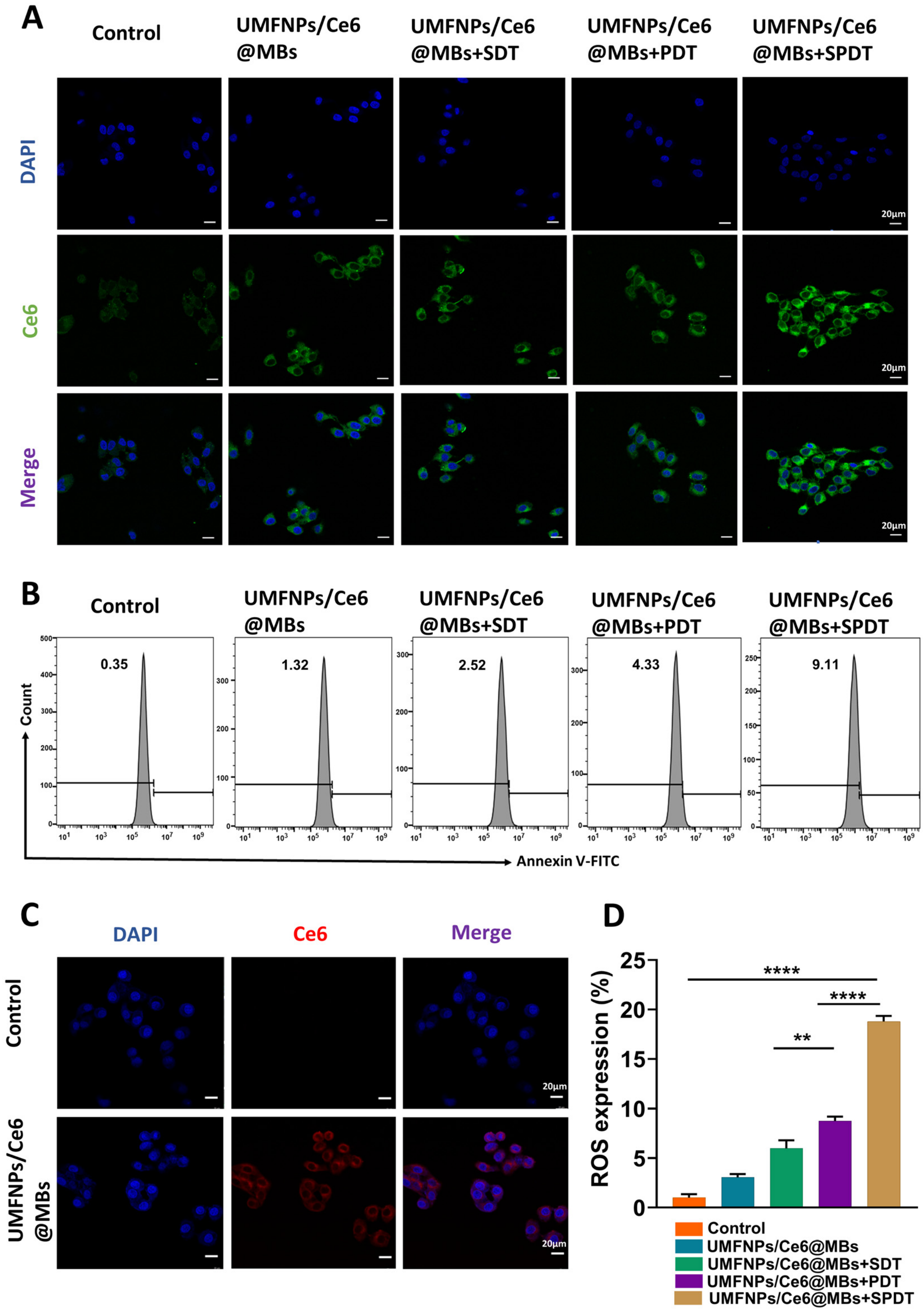

Fig. 3 *In vitro* treatment evaluation of UMFNPs/Ce6@MBs. (A and B) Quantitative evaluation of ROS generation by flow cytometry (n = 3). (C) Qualitative evaluation of ROS generation by confocal microscopy (scale bar: 20 μm). (D) Microbubble uptake by cells observed using a confocal microscope (scale bar: 20 μm). $^{**}p < 0.01$, $^{****}p < 0.0001$.

cant inflammation or injury. The inferior vena cava blood was collected from sacrificed mice, and centrifuged to obtain the serum to test hepatic function (*e.g.*, aspartate aminotransferase [AST/GOT] and alanine aminotransferase [ALT/GPT]) and renal function (*e.g.*, creatinine [CREA] and blood urea nitrogen [BUN]). Compared to the control group, there were no significant differences in hepatic function and renal function markers between the two groups (Fig. 4B), demonstrating that

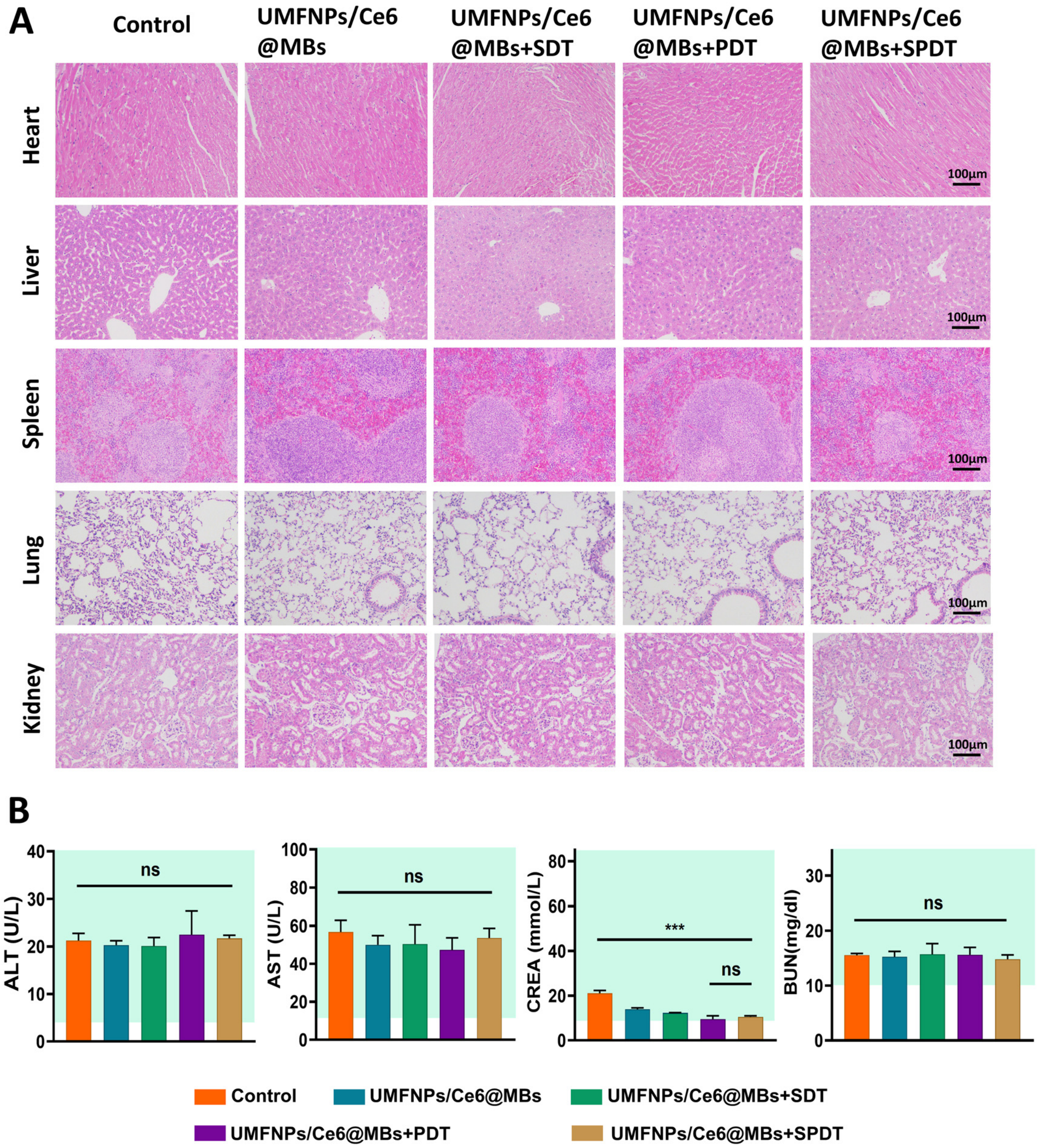

Fig. 4 *In vivo* safety assessment (n = 3). (A) HE-stained sections of organs and tumor tissues from different groups of mice after 2 weeks of treatment. (B) Markers of hepatic function (AST, ALT) and renal function (CREA, BUN) in different groups of mice after 2 weeks.

UMFNPs/Ce6@MBs did not produce any significant toxicity *in vivo*, confirming that the microbubbles are safe *in vivo*.

3.8. *In vivo* targeting and imaging results of UMFNPs/Ce6@MBs

UMFNPs/Ce6@MBs are microbubbles that can act as an ultrasound contrast agent for the real-time observation of contrast-enhanced ultrasound effect in the tumor site. As shown in Fig. 5A, the novel microbubbles showed good ultrasound imaging effects. At 1 min, the ultrasound contrast agent in the tumor site was the brightest and had the most potent effects. At 9 min, the contrast agent was metabolized in the tumor site. The microbubble-encapsulated Ce6 exhibits autofluorescence and can therefore be used for live animal imaging, allowing observation of the *in vivo* distribution and metabolism of microbubbles. To examine the *in vivo* distribution and metabolism of these microbubbles, we mainly imaged tumor-bearing mice at different time points (pre, 5 min, 30 min, 1 h, 4 h, 12 h, 24 h) (Fig. 5B). The microbubbles were found to be mainly enriched in the liver, kidneys, lungs, and tumor sites. At 30 min, they were mostly enriched in organs, tissues, and tumor sites, while after 30 min, they started to be metabolized *in vivo*. At 24 h, most microbubbles were metabolized. The other component encapsulated in microbubbles, UMFNPs, is a novel nanomaterial that can be used for MRI. As shown in Fig. 5C, this nanomaterial produces good MRI-T_1

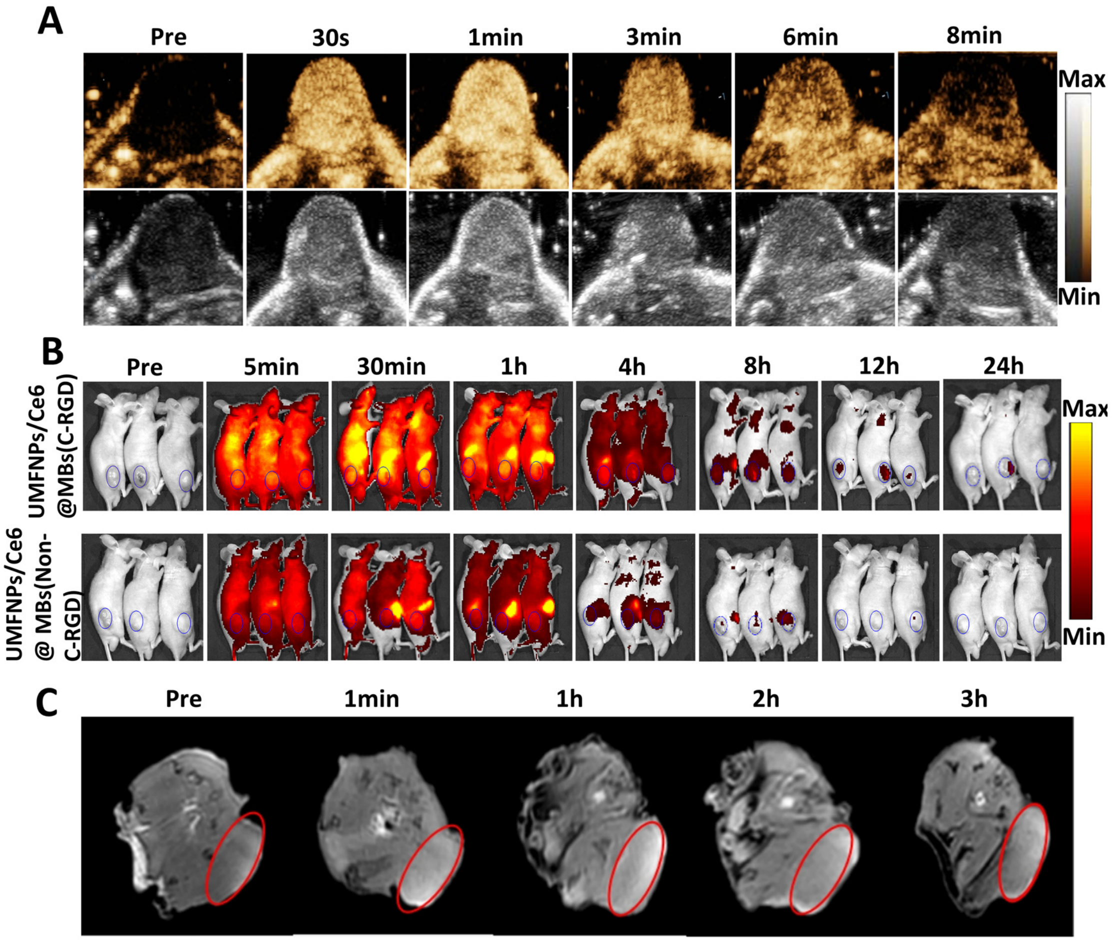

Fig. 5 *In vivo* distribution and imaging results of UMFNPs/Ce6@MBs. (A) Ultrasound images of UMFNPs/Ce6@MBs. (B) Animal FL images of UMFNPs/Ce6@MBs and UMFNPs/Ce6@MBs-(non-cRGD) modification. (C) *In vivo* MRI-T_1 images of UMFNPs/Ce6@MBs.

images. In summary, UMFNPs/Ce6@MBs can not only be used to diagnose lesions but also for the precise treatment of tumors. Therefore, UMFNPs/Ce6@MBs are stable microbubbles that combine diagnosis and precision treatment.

To better target tumors so that the drug is better utilized by the tumor, we modified microbubbles with C-RGD, a vascular integrin αvβ3 receptor. Furthermore, to examine its targeting effects, another group using the same encapsulated microbubble without C-RGD (UMFNPs/Ce6@MBs-(NonC-RGD)) modification was used for comparison. The targeting ability of the two groups was compared mainly by the fluorescence imaging effect *in vivo*. As shown in Fig. 5B and S2,† the fluorescence intensity of C-RGD-modified microbubbles *in vivo* imaging was stronger than that of the control group. Therefore, C-RGD-modified microbubbles have a better targeting effect than unmodified microbubbles.

3.9. *In vivo* treatment results

To examine the therapeutic effects of UMFNPs/Ce6@MBs combined with sono-photodynamic treatment on liver cancer, the mice were divided into the following six groups: blank control, model, UMFNP/Ce6@MB, UMFNP/Ce6@MB + SDT, UMFNP/Ce6@MB + PDT, and UMFNP/Ce6@MB + SPDT groups. The drug was administered by tail vein injection and treatment was conducted for 2 weeks. After 2 weeks of treatment, only four mice died in the UMFNP/Ce6@MB + PDT group, mainly due to the immunodeficient characteristics of nude mice, with poor immune tolerance. Additionally, the mice in the UMFNP/Ce6@MB + PDT group received intraperitoneal injection of anesthesia, whereas the other groups of mice received gaseous anesthesia; therefore, the UMFNP/Ce6@MB + PDT group was more prone to death. Dynamic changes in the body weight and tumor volume of mice were observed the day after treatment. The changes showed that the body weight of mice in the different groups was generally stable, with no significant change during the entire treatment course (Fig. 6A, S3†). The mouse tumor volume dynamic change results showed that the UMFNP/Ce6@MB + SPDT group had the best therapeutic effects, followed by the UMFNP/Ce6@MB + PDT and UMFNP/Ce6@MB + SDT groups. Compared to the model group, there were significant differences in therapeutic effects between the sono-photodynamic treatment group and the model group (Fig. 6B). After 2 weeks of treatment, the mice were sacrificed and the tumor tissues of tumor-bearing mice were dissected

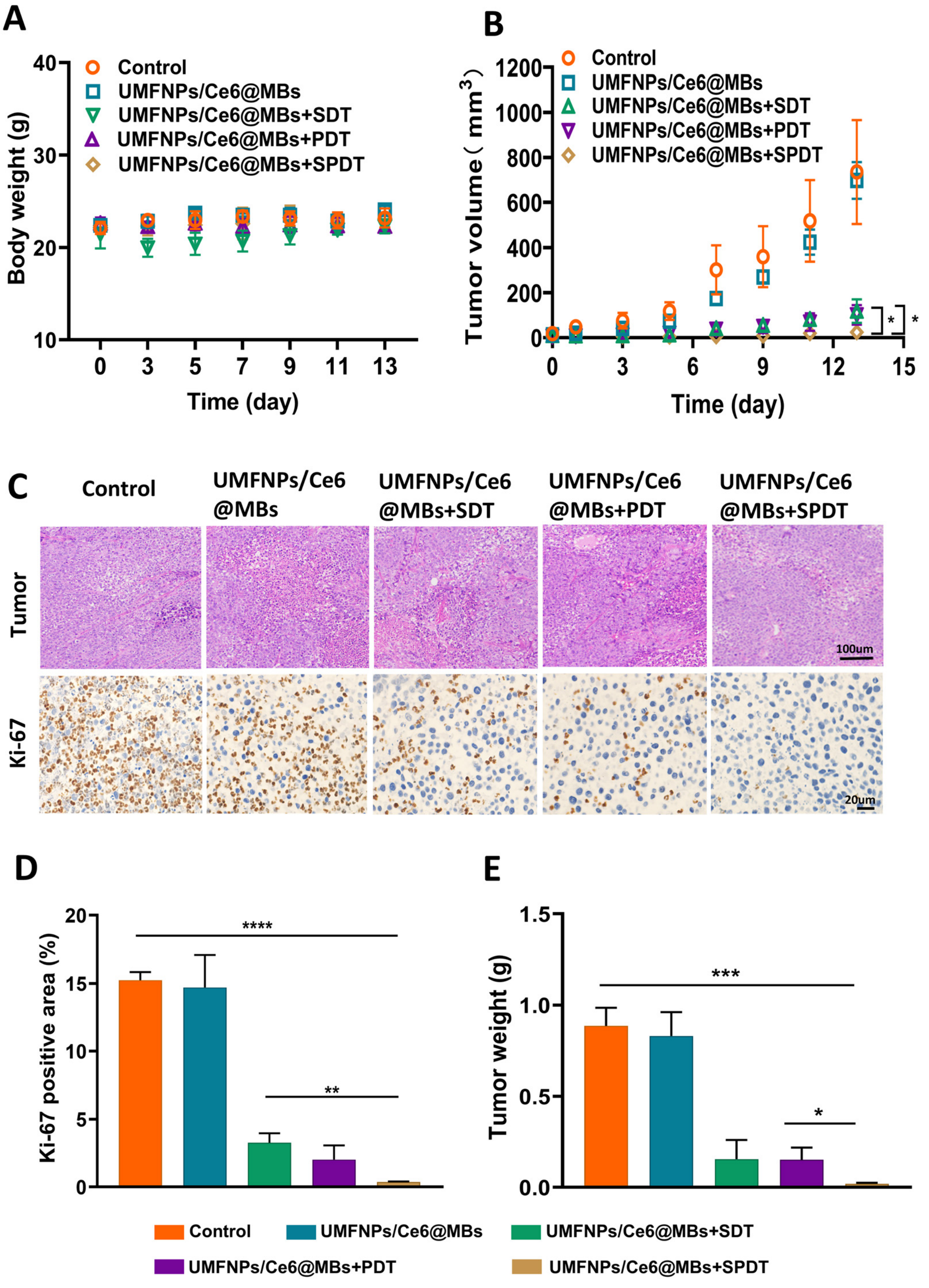

Fig. 6 *In vivo* treatment results. (A) Changes in the body weight of mice in different groups during the 2 weeks of treatment. (B) Changes in the tumor volume of mice in different groups during treatment. (C) HE and Ki-67 staining results of tumor tissues from mice in different groups after treatment. (D) Proportion of Ki-67-positive cells in the different groups. (E) Weight of dissected tumor tissues from different groups 2 weeks after treatment. *$p < 0.05$, **$p < 0.01$, ***$p < 0.001$, ****$p < 0.0001$.

and weighed. The results presented in Fig. 6E show that the tumor growth inhibition rates of the SDT, PDT, and SPDT groups were 83.91%, 90.15%, and 96.71%, respectively. Among them, the tumor growth in the UMFNP/Ce6@MB + SPDT group was significantly inhibited.

Ki-67 is a cell proliferation-related antigen associated with mitosis. The higher the level of tumor proliferation, the greater the Ki-67 expression. We next sectioned and stained the mouse tumor tissues, and the results are shown in Fig. 6C and D. The Ki-67 expression was found to be most significant in the model and UMFNP/Ce6@MB groups, whereas the intensity of brown staining was the lowest in the UMFNP/Ce6@MB + SPDT group, showing that the Ki-67 expression was the weakest in this group.

These results further demonstrate that UMFNPs/Ce6@MBs combined with sono-photodynamic treatment significantly inhibit tumor growth.

4. Discussion

In this study, we employed thin film hydration and mechanical vibration to prepare UMFNPs/Ce6@MB ultrasound microbubbles with a particle size of 1 μm (Fig. 1A–C) and a mean particle count of 4×10^{10} mL^{-1} (Fig. 1B). A previous study showed that microbubbles < 6 μm can pass through the lungs and capillaries *in vivo* and into the systemic circulation. After 24 h, most microbubbles were generally metabolized *in vivo* and did not cause cytotoxicity (Fig. 5B, S2†).[21] Therefore, the microbubbles prepared in this study have suitable particle sizes and quantities.

The sonoporation/ultrasound targeted microbubble destruction settings used in the *in vitro* experiment (frequency: 1.0 MHz, duty ratio: 20%, pulse frequency: 1000 Hz, magnetic reluctance intensity: 500 mW cm^{-2}, 1 min) were optimal parameters obtained through continuous adjustment. When the duty ratio is >20% or the magnetic reluctance intensity is >500 mW cm^{-2}, the cells will detach from the cell culture dishes, whereas a duty ratio <20% or magnetic reluctance intensity <500 mW cm^{-2} will result in suboptimal therapeutic effects.

During the whole process of conducting quantitative and qualitative experiments on ROS by cytometry and confocal microscopy, we found that the UMFNP/Ce6@MB group could produce weak fluorescence signals of ROS in both qualitative and quantitative experiments of ROS, despite efforts to perform experiments under the condition of avoiding light. This was due to the unavoidable influence of natural ambient light and the possible leakage of Ce from MB into cells, resulting in the qualitative and quantitative results of ROS in the simple microvesicle group (Fig. 3A and B). However, such effects were relatively small, and similar situations have been reported before.[22] Additionally, the CCK-8 assay results demonstrated that at a concentration of 15 μg mL^{-1}, the effects of combined sono-photodynamic treatment on the liver cancer cells were not as significant as those observed in the *in vivo* animal experiments. As shown in Fig. 3B, the inhibition rate of cell growth in the SPDT group was only 35.07%. However, in the animal experiments, the tumor growth inhibition rate of the SPDT group reached 96.71%. The cause of this difference may be the characteristics of the tumor microenvironment (TME), including the acidic pH, hypoxia, endogenous hydrogen peroxide (H_2O_2), and the high glutathione (GSH) level, which not only accelerate tumor progression and metastases but also drug resistance and treatment failure. However, previous studies have shown that various small-molecule drugs, enzymes, and functional nanomaterials can reverse the biological characteristics of the TME and play vital roles in improving cancer treatment.[23–26]

In this study, because of the unique physicochemical characteristics of nanoprobes within microbubbles (UMFNPs),[5] when microbubbles reach the tumor site and burst to release UMFNPs and Ce6, UMFNPs show good T_1-weighted MRI function *in vivo* (Fig. 5C). Simultaneously, the Mn^{2+} and Fe^{3+} ions in these nanoparticles are released and catalyze the degradation of hydrogen peroxide in the TME to fully produce O_2,[27] greatly increasing the intracellular $^1O_2$ level, thereby achieving satisfactory SDT and PDT efficiency both *in vivo* and *in vitro*, while the released Ce6 can be used for fluorescence imaging (Fig. 5B).[28] Our results showed that the novel ultrasound microbubbles exhibited good ultrasound imaging effects (Fig. 6A), achieving multimodal imaging that combines ultrasound, MRI-T_1, and fluorescence imaging. HCC can also be treated by combined ultrasound + laser under visualization guidance to obtain satisfactory therapeutic effects (Fig. 6A and E, S3†). In recent years, the demand for non-invasive, effective, and safe treatments has increased to improve tumor efficacy, leading SDT- and PDT-based treatments to gradually take center stage as research hotspots. PDT involves synergism between a non-toxic photosensitizer, oxygen, and harmless light to produce ROS to induce tumor cell death. ROS are intimately associated with vascular closure and immune system activation.[29] Because commonly used photosensitizers (with porphyrinyl groups) have a low tissue penetration depth of light, the use of PDT is restricted to superficial cancers and is poorly utilized. Therefore, an increasing number of nanophotosensitizers have been successively developed.[30] PDT can be combined with SDT, chemodynamic therapy (CDT), and photothermal therapy (PTT) to maximize the therapeutic effects of PDT in cancer.[31] SDT is a promising cancer treatment based on the synergism between low-intensity ultrasound, sonosensitizer, and molecular oxygen ($^3O_2$). Its mechanisms may be related to ultrasound vacuolation, cancer cell apoptosis, ultrasonic thermal effect, and antitumor immunity, and the high penetration of sound and the sonosensitizer is used to produce ROS.[18] SDT has proven efficacy as an anticancer treatment, with good safety, sufficient tissue penetration depth, high therapeutic efficacy, few side effects, and low cost; hence, it has good clinical application prospects.[32–35] Some researchers have combined SDT, nanotechnology (another research hotspot), and immunotherapy, whereby the resulting synergism not only effectively inhibits primary tumor growth but also induces strong tumor-specific immune responses to suppress distal unirradiated tumors.[36]

Many researchers have made great efforts to improve the efficacy of treatments for liver cancer. For example, Jae Sun Park *et al.* used a photosensitizer (indocyanine green) with a strong absorption peak in the 808 nm near-infrared region for PDT combined with chemotherapy (sorafenib or doxorubicin) to treat liver cancer and obtained good results, showing that the tumors of PDoX mice treated with both PDT and chemotherapy had completely shrank by day 26. In addition, PDT can help alleviate sorafenib-induced dermotoxicity.[37] Some researchers have also combined SDT with nanoparticles to treat liver cancer. Indeed, Lin *et al.* designed ultrasound and glutathione (GSH) dual responsive vesicles of Janus Au–MnO nanoparticles (JNPs) coated with PEG and a ROS-sensitive polymer to treat liver cancer. A novel sound-sensitive nanovesicle was developed by self-assembly to increase nanodrug penetration in primary liver tumors, and tumor growth was suppressed through enhanced SDT and CDT synergism.[38] Some researchers have even constructed multifunctional nanoplatforms with targeting effects for image-guided precision diagnosis and photothermal/photodynamic treatment of primary liver cancer.[39,40]

In this study, we designed and developed a TME-responsive multifunctional cancer treatment nanoplatform ultrasound microbubble (UMFNPs/Ce6@MBs) whose surface was modified by a cyclic peptide (C-RGD) to better target integrin αvβ3 on the tumor blood vessel surfaces.[41] We employed multimodal imaging in liver cancer diagnosis and used SPDT to treat liver cancer. The results showed that SPDT significantly inhibited tumor growth, with better efficacy than the SDT and PDT groups, thereby achieving precision diagnosis and treatment.

5. Conclusions

In conclusion, we have successfully developed a multifunctional nanotherapeutic diagnostic platform UMFNPs/Ce6@MBs to enhance the precision diagnosis and treatment of HCC. UMFNPs/Ce6@MBs modified with cRGD have strong targeting performance and can accurately deliver Ce6 to the tumor site and release it precisely under ultrasonic irradiation. In addition, UMFNPs/Ce6@MBs can produce O_2 in response to the tumor microenvironment (H_2O_2/pH), which can relieve hypoxia by increasing the production of ROS. Enhanced SPDT can effectively inhibit the growth of hepatoma Huh-7 cells and successfully inhibit the proliferation of tumor tissue. UMFNPs/Ce6@MBs, which are composed of Mn^{2+}, Ce6 and microvesicle contrast agents, show high performance multi-modal imaging function in FL/MR/US imaging and are used for accurate diagnosis and treatment guidance of liver cancer.

Author contributions

Manuscript drafting, data curation, investigation, and visualization: Lijun Xing, Xiaoting Yang, Jianhua Bai, Bingxuan Xu, and Jing Cai; methodology, validation, and project administration: Qing Dan and Bingxuan Xu; *in vitro* experiments: Lijun Xing, Xiaoting Yang, Jianhua Bai and Bingxuan Xu; *in vivo* imaging experiments: Lijun Xing, Yiran Ji, Chunting Zhong, Keyan Yu and Yulong Qi; *in vivo* anti-cancer experiments: Lijun Xing, Xiaoting Yang, Jianhua Bai, Bingxuan Xu and Xiaoyu Chen; study design and conceptualization: Tingting Zheng and Li Liu; supplementary experimental data: Chunting Zhong, Xiaoting Yang, and Jianhua Bai; resources and funding acquisition: Li Liu, Yun Chen, Tingting Zheng and Li Li; supervision and manuscript editing: Tingting Zheng and Xintao Shuai. All authors have approved the manuscript and agreed with its submission to Biomaterials Science.

Ethical statement

All procedures were approved by the Animal Use and Care Committee of Shenzhen Peking University-The Hong Kong University of Science and Technology Medical Center (SPHMC) with the NIH Guidelines for the Care and Use of Laboratory Animals and Public Health Policy (protocol number 2020-032).

Data availability

All data generated or analysed during this study are included in this published article and its ESI files.†

Conflicts of interest

There are no conflicts to declare.

Acknowledgements

Li Liu thanks the funders of JCYJ20200109140212277, JCYJ20210324110211031 and JCYJ20210324105614038 for their support; Yun Chen thanks the funders of KCXFZ202002011010487 and 2022A1515010296 for their support; Tingting Zheng thanks the funders of 2022A1515010986 and JCYJ20210324131402008 for their support; and all authors thank the funders of SZSM202111011 and SZXK051 for their support. We also thank the Post-doctoral Station for providing deep research start-up funds for their support. In addition, we also thank the Shenzhen-Peking University-Hong Kong University of Science and Technology Medical Center for facility support and The LetPub (**https://www.letpub.com**) for providing language assistance during the drafting of this manuscript.

References

1 W. Cao, H.-D. Chen, Y.-W. Yu, N. Li and W.-Q. Chen, *Chin. Med. J.*, 2021, **134**, 783–791.
2 M. Iranshahy, R. Rezaee and G. Karimi, *Eur. J. Pharmacol.*, 2019, **850**, 1–7.
3 D. Anwanwan, S. K. Singh, S. Singh, V. Saikam and R. Singh, *Biochim. Biophys. Acta, Rev. Cancer*, 2020, **1873**, 188314.
4 F. Graur, A. Puia, E. I. Mois, S. Moldovan, A. Pusta, C. Cristea, S. Cavalu, C. Puia and N. Al Hajjar, *Materials*, 2022, **15**, 3893.

5 S. Xiao, X. Yu, L. Zhang, Y. Zhang, W. Fan, T. Sun, C. Zhou, Y. Liu, Y. Liu, M. Gong and D. Zhang, *Int. J. Nanomed.*, 2019, **14**, 8499–8507.

6 H. Zhang, L. Li, X. L. Liu, J. Jiao, C. T. Ng, J. B. Yi, Y. E. Luo, B. H. Bay, L. Y. Zhao, M. L. Peng, N. Gu and H. M. Fan, *ACS Nano*, 2017, **11**, 3614–3631.

7 Q. Mei, M. Yu and Q. Chen, *World J. Clin. Cases*, 2022, **10**, 8525–8534.

8 A. Singal, M. L. Volk, A. Waljee, R. Salgia, P. Higgins, M. A. Rogers and J. A. Marrero, *Aliment. Pharmacol. Ther.*, 2009, **30**, 37–47.

9 J. H. Correia, J. A. Rodrigues, S. Pimenta, T. Dong and Z. Yang, *Pharmaceutics*, 2021, **13**, 1332.

10 E. C. Cheung and K. H. Vousden, *Nat. Rev. Cancer*, 2022, **22**, 280–297.

11 T. H. Hu, J. C. Wu, S. T. Huang, T. H. Chu, A. J. Han, T. W. Shih, Y. C. Chang, S. M. Yang, C. Y. Ko, Y. W. Lin, M. L. Kung and M. H. Tai, *J. Biol. Chem.*, 2023, 105335, DOI: **10.1016/j.jbc.2023.105335**.

12 H. Mirzaei, G. E. Djavid, M. Hadizadeh, M. Jahanshiri-Moghadam and P. Hajian, *J. Photochem. Photobiol., B*, 2015, **142**, 86–91.

13 G. C. de Miguel, A. M. Abrantes, M. Laranjo, A. Y. K. Grizotto, B. Camporeze, J. A. Pereira, G. Brites, A. Serra, M. Pineiro, A. Rocha-Gonsalves, M. F. Botelho and D. G. Priolli, *Photodiagn. Photodyn. Ther.*, 2018, **21**, 79–85.

14 S. Fan, Y. Zhang, H. Tan, C. Xue, Y. He, X. Wei, Y. Zha, J. Niu, Y. Liu, Y. Cheng and D. Cui, *Nanoscale*, 2021, **13**, 5383–5399.

15 Q. Chen, J. Huang, Y. Ye, A. Hu, B. Xu, D. Hu, L. Wang, L. Xing, S. Chen, X. Gui, W. Tong, Y. Gan, T. Zheng, J. Zheng, L. Liu and G. Hu, *J. Controlled Release*, 2023, **358**, 319–332.

16 Z. Zhang, B. Xu, T. Lv, Y. Shi, M. Wang, D. Hu, A. Hu, P. Li, S. Lin and S. Zhang, *Adv. Ther.*, 2023, **6**, 2300056.

17 Z. Zhao, X. Lin, L. Zhang, X. Liu, Q. Wang, Y. Shi, G. Cui, H. Cai, Y. Chen, Y. Li, A. Hu, Z. Zhang, J. Liu, H. Xie, T. Zheng, X. Liang, X. Shuai, Y. Chen and D. Sun, *J. Biomed. Nanotechnol.*, 2021, **17**, 1293–1304.

18 P. Li, X. Tan, Q. Dan, A. Hu, Z. Hu, X. Yang, J. Bai, X. Chen, B. Li, G. Cheng, L. Liu, Y. Chen, D. Sun, X. Shuai and T. Zheng, *Biomater. Sci.*, 2024, **12**, 1465–1476.

19 S. Guo, Z. Zhang, B. Xu, M. Wang, T. Fan, X. Zhong, A. Hu, D. Hu, L. Luo, S. Lin, L. Wang, R. Yao, J. Huang, H. Hu, X. Shuai, J. Shi, Y. Chen and T. Zheng, *Adv. Ther.*, 2024, **7**, 2300254.

20 Y. Miao, Q. Xie, H. Zhang, J. Cai, X. Liu, J. Jiao, S. Hu, A. Ghosal, Y. Yang and H. Fan, *Theranostics*, 2019, **9**, 1764–1776.

21 Z. Ma, J. Liu, X. Li, Y. Xu, D. Liu, H. He, Y. Wang and X. Tang, *Drug Delivery Transl. Res.*, 2022, **12**, 306–324.

22 J. X. Zhu, W. T. Zhu, J. H. Hu, W. Yang, P. Liu, Q. H. Liu, Y. X. Bai and R. Xie, *Ultrasound Med. Biol.*, 2020, **46**, 2030–2043.

23 G. Yang, J. Ji and Z. Liu, *Wiley Interdiscip. Rev.: Nanomed. Nanobiotechnol.*, 2021, **13**, e1720.

24 I. Vitale, G. Manic, L. M. Coussens, G. Kroemer and L. Galluzzi, *Cell Metab.*, 2019, **30**, 36–50.

25 X. Liu, Y. Hao, R. Popovtzer, L. Feng and Z. Liu, *Adv. Healthc. Mater.*, 2021, **10**, e2001167.

26 P. Zhang, Q. Wu, J. Yang, M. Hou, B. Zheng, J. Xu, Y. Chai, L. Xiong and C. Zhang, *Acta Biomater.*, 2022, **146**, 450–464.

27 Q. Xu, G. Zhan, Z. Zhang, T. Yong, X. Yang and L. Gan, *Theranostics*, 2021, **11**, 1937–1952.

28 S. Sun, J. Chen, K. Jiang, Z. Tang, Y. Wang, Z. Li, C. Liu, A. Wu and H. Lin, *ACS Appl. Mater. Interfaces*, 2019, **11**, 5791–5803.

29 R. Baskaran, J. Lee and S. G. Yang, *Biomater. Res.*, 2018, **22**, 25.

30 A. Kumar, M. Sharipov, A. Turaev, S. Azizov, I. Azizov, E. Makhado, A. Rahdar, D. Kumar and S. Pandey, *Polymers*, 2022, **14**, 3027.

31 J. Hu, J. Shi, Y. Gao, W. Yang, P. Liu, Q. Liu, F. He, C. Wang, T. Li, R. Xie, J. Zhu and P. Yang, *Int. J. Nanomed.*, 2019, **14**, 10009–10021.

32 H. Q. Dong, X. F. Fu, M. Y. Wang and J. Zhu, *World J. Clin. Cases*, 2023, **11**, 5193–5203.

33 F. Qu, P. Wang, K. Zhang, Y. Shi, Y. Li, C. Li, J. Lu, Q. Liu and X. Wang, *Autophagy*, 2020, **16**, 1413–1435.

34 G. Canavese, A. Ancona, L. Racca, M. Canta, B. Dumontel, F. Barbaresco, T. Limongi and V. Cauda, *Chem. Eng. J.*, 2018, **340**, 155–172.

35 L. Rengeng, Z. Qianyu, L. Yuehong, P. Zhongzhong and L. Libo, *Photodiagn. Photodyn. Ther.*, 2017, **19**, 159–166.

36 X. Lin, R. Huang, Y. Huang, K. Wang, H. Li, Y. Bao, C. Wu, Y. Zhang, X. Tian and X. Wang, *Int. J. Nanomed.*, 2021, **16**, 1889–1899.

37 J. S. Park, S. Park, S. J. Park and S. K. Kim, *J. Photochem. Photobiol., B*, 2023, **239**, 112642.

38 X. Lin, S. Liu, X. Zhang, R. Zhu, S. Chen, X. Chen, J. Song and H. Yang, *Angew. Chem., Int. Ed.*, 2020, **59**, 1682–1688.

39 S. Qi, G. Liu, J. Chen, P. Cao, X. Lei, C. Ding, G. Chen, Y. Zhang and L. Wang, *Int. J. Nanomed.*, 2022, **17**, 3777–3792.

40 D. Zhao, J. Cao, L. Zhang, S. Zhang and S. Wu, *Biosensors*, 2022, **12**, 342.

41 X. Q. Chen, M. Liu, R. F. Wang, P. Yan, C. L. Zhang, C. Ma, Q. Zhao, L. Yin, G. Y. Zhao and F. Q. Guo, *J. Labelled Compd. Radiopharm.*, 2017, **60**, 385–393.